Commun. Comput. Phys.
doi: 10.4208/cicp.110310.090911a

Vol. **11**, No. 5, pp. 1697-1717
May 2012

Parareal in Time Simulation of Morphological Transformation in Cubic Alloys with Spatially Dependent Composition

Li-Ping He* and Minxin He

Department of Mathematics, Shanghai Jiaotong University, Shanghai 200240, China.

Received 11 March 2010; Accepted (in revised version) 9 September 2011

Communicated by Longqing Chen

Available online 12 January 2012

Abstract. In this paper, a reduced morphological transformation model with spatially dependent composition and elastic modulus is considered. The parareal in time algorithm introduced by Lions et al. is developed for longer-time simulation. The fine solver is based on a second-order scheme in reciprocal space, and the coarse solver is based on a multi-model backward Euler scheme, which is fast and less expensive. Numerical simulations concerning the composition with a random noise and a discontinuous curve are performed. Some microstructure characteristics at very low temperature are obtained by a variable temperature technique.

AMS subject classifications: 52B10, 65D18, 68U05, 68U07

Key words: Morphological transformation, multi-model scheme, parareal in time simulation.

1 Introduction

Many time-stepping methods have been developed for phase field models. Several explicit and implicit finite element schemes of the Cahn-Hilliard model were studied with mathematical rigor by Barrett et al. [3], Feng and Prohl [15], Elliott et al. [9–12]. Wang and Khachaturyan [35] considered Euler method for the three-dimensional field model of martensitic transformations. The semi-implicit Fourier spectral method for the Cahn-Hilliard model was proposed by Chen and Shen [5]. The large time-stepping semi-implicit methods for epitaxial growth models were proposed by Xu and Tang [40], and the Gauss-Seidel projection finite difference method of micromagnetics model was developed by Wang et al. [38]. For the phase field crystal model, Cheng [6] proposed an efficient algorithm, while Wu et al. [39] developed the stable difference nonlinear-multigrid

*Corresponding author. *Email addresses:* lphe@sjtu.edu.cn (L.-P. He), sophiaminxinhe@gmail.com (M. He)

method. In resent studies, see, e.g., [13,14,34], the unconditionally stable algorithms were developed for the Cahn-Hilliard equation. These algorithms allow for an increasing time step in Cahn-Hilliard systems as time proceeds.

In this paper, we consider the strain-induced morphological transformation model of cubic alloys, in which the composition and elastic modulus are spatially dependent. This model was proposed by Wang et al. [36] and developed by [27,28,30–33,37,41–44] where it is assumed that the composition and elastic modulus are positive constant. The advantages of such a model is the effects of coherent elastic strains on the kinetics of morphological transformations in solid state precipitation without any a prior assumptions on the possible morphologies that could develop, and an nonstructural decomposition of a cubic disordered phases in a binary alloy is then carried out. But we meet several difficulties in simulations. For instance, how to deal with the model if the composition includes a random noise or a discontinuous curve. As we only obtain an explicit representation of the model in reciprocal space (we can not derive its explicit one in physical space), solving the nonlinear equation at each time step becomes much more expensive. To overcome the difficulties mentioned above, we shall consider the reduction method for the morphological transformation model and numerical techniques. The possible contributions of this work are (i) the reduced morphological transformation model in dimensionless form is derived; (ii) the multi-model backward Euler scheme is developed, which is fast and inexpensive; (iii) a variable temperature model with numerical techniques are given; in particular, numerical simulations concerning the microstructure characteristic at very low temperature are performed; and (iv) the parareal in time algorithm is achieved for longer-term simulation.

This paper is organized as follows: In Section 2 the Önsager equation with spatially dependent composition and elastic modulus is shown. Section 3 derives the reduced morphological transformation model. Section 4 develops the multi-model method and variable temperature technique, and the offline-online procedures are discussed. Moreover, numerical simulations concerning the composition with a random noise and a discontinuous curve are reported. Section 5 is devoted to the parareal in time algorithm. Finally, we give some conclusions in Section 6.

2 Kinetic equation with spatially dependent composition

2.1 The Önsager equation

Let $c(\boldsymbol{r})$ be the atomic fraction of solute atoms, K_B be the Boltzmann's constant, T be the absolute temperature, $\lambda(\boldsymbol{r}-\boldsymbol{r}')$ be a matrix of kinetic coefficients related to probabilities of elementary diffusional jumps from lattice site $\boldsymbol{r}$ to $\boldsymbol{r}'$ of a Bravais lattice during a time unit, and $\mathcal{F}_{\text{ree}}$ be the total free energy including the strain energy contribution. Then it is well know that the crystal lattice site diffusion in a binary substitution alloy is determined by a diffusible relaxation of the nonequilibrium single site occupation probability of a solute atom at crystal lattice site $\boldsymbol{r}$ and at time t, which is denoted by $\eta(\boldsymbol{r},t)$ and satisfies the

following Önsager equation (see [36])

$$\frac{\partial\eta(\boldsymbol{r},t)}{\partial t}=\frac{1}{K_BT}\sum_{\boldsymbol{r}'}\lambda(\boldsymbol{r}-\boldsymbol{r}')\left\{c(\boldsymbol{r}')(1-c(\boldsymbol{r}'))\frac{\delta\mathcal{F}_{\rm ree}}{\delta\eta(\boldsymbol{r}',t)}\right\},\quad \boldsymbol{r}\in\Omega, \tag{2.1}$$

where the summation over $\boldsymbol{r}'$ is carried out over all $\boldsymbol{N}$ lattice sites of a crystal. Clearly, its Fourier representation is as follows

$$\frac{\partial\widetilde{\eta}(\boldsymbol{k},t)}{\partial t}=\frac{1}{K_BT}\widetilde{\lambda}(\boldsymbol{k})\left\{\widetilde{G}_T(\eta(\boldsymbol{r},t))\right\}_{\boldsymbol{k}}, \tag{2.2}$$

where $\boldsymbol{k}$ is the reciprocal lattice vector, $\widetilde{\lambda}(\boldsymbol{k})$ and $\{\widetilde{G}_T(\eta(\boldsymbol{r},t))\}_{\boldsymbol{k}}$ are the Fourier transforms of the corresponding real space function $\lambda(\boldsymbol{r})$ and the nonlinear term

$$G_T(\eta(\boldsymbol{r},t))=c(\boldsymbol{r})(1-c(\boldsymbol{r}))\frac{\delta\mathcal{F}_{\rm ree}}{\delta\eta(\boldsymbol{r},t)}, \tag{2.3}$$

respectively. In the system, the conservation of atoms is described by

$$\sum_{\boldsymbol{r}}\lambda(\boldsymbol{r}-\boldsymbol{r}')=0.$$

In the case of an ideal solid solution, the Önsager equation describes a random walk problem, and while in the long-wave approximation, it leads to the conventional Cahn-Hilliard equation.

2.2 Khachaturyan's elastic strain energy

According to the Khachaturyan microscopic elasticity theory [18], the strain energy of a binary solid solution is composed of different two parts: (i) the conflagrations independent term describing the self-energy and image force induced energy, which is not affected by spatial redistribution of solute atoms and therefore it can be ignored; (ii) the configuration dependent term associated with concentration inhomogeneity, which leads to a substantially nonlocal strain energy change associated with spatial distribution of solute atoms. Also, such a strain energy depends on the volume of the precipitate phase, and thus it describe the main characteristic in the structural transformations.

For a cubic substitution solid solution, solute atoms are dilatational centers and their introduction leads to an isotropic crystal lattice expansion characterized by a stress-free strain tensor $\epsilon^0_{ij}=\epsilon_0\delta_{ij}$, where $\epsilon_0=\mathrm{d}a/a\ \mathrm{d}c(\boldsymbol{r})$ is the concentration coefficient of crystal lattice expansion caused by the atomic size difference, a is the crystal lattice parameter of a solid solution, $c(\boldsymbol{r})$ is the atomic fraction of solute atoms and δ_{ij} is the Kronecker delta symbol. Under these conditions, the configuration dependent strain energy associated with an arbitrary distribution $\eta(\boldsymbol{r})$ is defined as

$$E_{\rm el}=\frac{1}{2N}\sum_{\boldsymbol{k}\neq0}v(\boldsymbol{k})_{\rm el}|\widetilde{\eta}(\boldsymbol{k})|^2, \tag{2.4}$$

where $v(\boldsymbol{k})_{\rm el}$ is the Fourier transform of the infinite radius strain induced interaction energy $\omega(\boldsymbol{r})_{\rm el}$, and $\widetilde{\eta}(\boldsymbol{k})$ is the Fourier transform of $\eta(\boldsymbol{r})$. Since a decomposition process is determined by development of a packet of concentration waves with wave vectors close to zero, the long-wave approximation for $v(\boldsymbol{k})$ becomes

$$v(\boldsymbol{k})_{\rm el}\approx\kappa(\boldsymbol{e})=-\sigma_0^2[e_i\Omega(\boldsymbol{e})_{ij}e_j-\langle e_i\Omega(\boldsymbol{e})_{ij}e_j\rangle_e], \tag{2.5}$$

where $\sigma_0=(c_{11}+2c_{12})\epsilon_0$, c_{11} and c_{12} are elastic constants of a cubic crystal, $\boldsymbol{e}=\boldsymbol{k}/|\boldsymbol{k}|$ is a unit vector in the $\boldsymbol{k}$ direction, $\Omega(\boldsymbol{e})_{ij}$ is a Green tensor reciprocal to $C_{ijkl}e_ke_l$ (C_{ijkl} is a tensor of the elastic constants) and $\langle\cdots\rangle_e$ is a symbol of averaging over all directions $\boldsymbol{k}$. In (2.5), the Einstein suffix notation is used. At $\boldsymbol{k}=0$, as $\boldsymbol{k}\to 0$ depends on the $\boldsymbol{k}$ direction. This singularity results in a long-range asymptotic behavior of the strain induced interaction in real space (see [36]). Rewriting Eq. (2.4) in a real space representation brings

$$E_{\rm el}=\frac{1}{2}\sum_{\boldsymbol{r}\boldsymbol{r}'}\omega(\boldsymbol{r}-\boldsymbol{r}')_{\rm el}\eta(\boldsymbol{r})\eta(\boldsymbol{r}'). \tag{2.6}$$

2.3 Variational derivative

Now the free energy for an inhomogeneous solid solution reads as follows:

$$\mathcal{F}_{\rm ree}=\frac{1}{2}\sum_{\boldsymbol{r}\boldsymbol{r}'}\omega(\boldsymbol{r}-\boldsymbol{r}')\eta(\boldsymbol{r})\eta(\boldsymbol{r}')+K_BT\sum_{\boldsymbol{r}}\Big(\eta(\boldsymbol{r})\ln\eta(\boldsymbol{r})+(1-\eta(\boldsymbol{r}))\ln(1-\eta(\boldsymbol{r}))\Big), \tag{2.7}$$

where

$$\omega(\boldsymbol{r}-\boldsymbol{r}')=\omega(\boldsymbol{r}-\boldsymbol{r}')_{\rm f}+\omega(\boldsymbol{r}-\boldsymbol{r}')_{\rm el}$$

is a pairwise interaction energy between two atoms at lattice sites $\boldsymbol{r}$ and $\boldsymbol{r}'$, in which $\omega(\boldsymbol{r}-\boldsymbol{r}')_{\rm f}$ describes the finite radius interaction, and $\omega(\boldsymbol{r}-\boldsymbol{r}')_{\rm el}$ describes the infinite radius strain-induced interaction. It is safe to assume that the mechanical equilibrium in a system is established much faster than any diffusion processes. As a result, the system is always at mechanical equilibrium during phase separation or during coarsening. Therefore, at each time step, the mechanical equilibrium equations have to be solved either numerically or analytically. It was shown by Khachaturyan that, in the homogeneous modulus approximation, the elastic energy of any arbitrary microstructure can be analytically calculated. However, the elastic energy is a double-volume integral of infinitely long-ranged elastic interactions in real space, and its contribution to the total driving force enters Eq. (2.1) as a volume integral, a nonlocal term (see [36]). Therefore, direct numerical solution in the real space is prohibitively difficult. In the Fourier space, the elastic energy is reduced to a single volume integral of the Fourier transform of the elastic interactions. Let $\Big\{\widetilde{\frac{\delta\mathcal{F}_{\rm ree}}{\delta\eta(\boldsymbol{r},t)}}\Big\}_{\boldsymbol{k}}$ be the Fourier transforms of the real space function $\frac{\delta\mathcal{F}_{\rm ree}}{\delta\eta(\boldsymbol{r},t)}$,

$$\kappa(\boldsymbol{e})=\sum_{\boldsymbol{r}}\omega(\boldsymbol{r})_{\rm el}\exp(-i\boldsymbol{k}\boldsymbol{r}),\quad v(\boldsymbol{k})_{\rm f}=\sum_{\boldsymbol{r}}\omega(\boldsymbol{r})_{\rm f}\exp(-i\boldsymbol{k}\boldsymbol{r}), \tag{2.8}$$

and $v(\boldsymbol{k})=\sum_{\boldsymbol{r}}[\omega(\boldsymbol{r})_{\rm f}+\omega(\boldsymbol{r})_{\rm el}]\exp(-i\boldsymbol{k}\boldsymbol{r})$. Obviously,

$$v(\boldsymbol{k})=v(\boldsymbol{k})_{\rm f}+\kappa(\boldsymbol{e}), \tag{2.9}$$

from which the Fourier transform of the variational derivatives becomes

$$\left\{\widetilde{\frac{\delta\mathcal{F}_{\rm ree}}{\delta\eta(\boldsymbol{r},t)}}\right\}_{\boldsymbol{k}}=\big(v(\boldsymbol{k})_{\rm f}+\kappa(\boldsymbol{e})\big)\widetilde{\eta}(\boldsymbol{k},t)+K_BT\left\{\widetilde{\phi}(\eta(\boldsymbol{r},t))\right\}_{\boldsymbol{k}},$$

where $\{\widetilde{\phi}(\eta(\boldsymbol{r},t))\}_{\boldsymbol{k}}$ is the Fourier transforms of the real space function

$$\phi(\eta(\boldsymbol{r},t))=\ln\left(\frac{\eta(\boldsymbol{r},t)}{1-\eta(\boldsymbol{r},t)}\right). \tag{2.10}$$

3 The reduced model

3.1 Basic assumption

In this paper, we consider two-dimensional (2D) periodic binary substitutional solid solution of an nonstructural decomposition in a square lattice consisting of $\boldsymbol{N}=N\times N$ unit cells. A coherency between the precipitate and matrix phases is assumed. Also, we assume that the two disordered product phases have the same disordered structure and elastic modula, but different compositions and thus different crystal lattice parameters.

By assumed atomic jumps between only nearest neighbor sites and using the condition that the total number of atoms in the system are conserved, i.e., $\sum_{\boldsymbol{r}}\lambda(\boldsymbol{r})=0$, for a f.c.c. lattice, the function $\tilde{\lambda}(\boldsymbol{k})$ in (2.2) now can be written as

$$\tilde{\lambda}(\boldsymbol{k})=-2\lambda_1(2-\cos k_xa-\cos k_ya), \tag{3.1}$$

where λ_1 is proportional to the jump probability between the nearest-neighbor sites at a time unit.

The interaction energies of the system are chosen in such a way that leads to an construction decomposition when the system is quenched to a lower temperature. Hence, we assume that

$$v(0)_{\rm f}=\min[v(\boldsymbol{k})_{\rm f}].$$

Since $v(\boldsymbol{k})_{\rm f}$ describes the finite radius atomic interaction, its back Fourier transform, the interchange energies $\omega(\boldsymbol{r})_{\rm f}$, have non-vanishing values only for a few coordination shells. Therefore the interactions beyond the second coordination shell shall be assumed to be zero. Now denote by a the crystal lattice parameter, and by $\omega_1\leq 0$ and $\omega_2\leq 0$ the nearest and next nearest neighbor pairwise interchange energies, which are assumed satisfying

$$\omega_1=\gamma\omega_2,\quad \gamma>0. \tag{3.2}$$

Thus the function $v(\boldsymbol{k})_{\rm f}$ in a 2-neighbor interaction model can be written as

$$v(\boldsymbol{k})_{\rm f}=\omega_1(\cos k_x a+\cos k_y a)+\beta\omega_2\cos k_x a\cos k_y a, \tag{3.3}$$

where $\beta\geq 0$ and $\boldsymbol{k}=(k_x,k_y)$, in which k_x and k_y are components of the vector $\boldsymbol{k}$ along the x and y axes to the $\{10\}$ and $\{01\}$ directions in the reciprocal space.

The infinite radius strain-induced interaction described by Eq. (2.6) can be approximated as

$$\kappa(\boldsymbol{e})\approx\kappa_0\left(e_x^2e_y^2-\frac{1}{8}\right), \tag{3.4}$$

where e_x and e_y are components of the unit vector $\boldsymbol{e}$ along the x and y axes in the reciprocal space and κ_0 is a material constant. In our simulation $\kappa_0>0$ which occurs for alloys with a negative elastic anisotropy. The term $1/8$ in (3.4) is $\langle e_x^2e_y^2\rangle$.

3.2 Dimensionless form

Let $\eta(\boldsymbol{r},t)\to c(\boldsymbol{r})$ in (2.7). Then the phase diagram can be obtained by minimizing the free energy

$$\mathcal{F}_{\rm ree}=N^2\left[\frac{1}{2}v(0)c^2(\boldsymbol{r})+K_BT(c(\boldsymbol{r})\ln c(\boldsymbol{r})+(1-c(\boldsymbol{r}))\ln(1-c(\boldsymbol{r})))\right].$$

Since $\kappa(\boldsymbol{e})$ has a singularity at $\boldsymbol{k}=0$, we take

$$\min[v(\boldsymbol{k})]\approx v(0)_{\rm f}+\kappa(\boldsymbol{e_0}),$$

where $\kappa(\boldsymbol{e_0})=\min[\kappa(\boldsymbol{e})]$, in which $\boldsymbol{e_0}=\langle 01\rangle$. From (3.4), we see that $\kappa(\boldsymbol{e_0})=-\kappa_0/8$. Thus the stable coherent diagram can be determined from the free energy

$$\mathcal{F}_{\rm ree}=N^2\left[\frac{1}{2}(v(0)_{\rm f}-\kappa_0/8)c^2(\boldsymbol{r})+K_BT(c(\boldsymbol{r})\ln c(\boldsymbol{r})+(1-c(\boldsymbol{r}))\ln(1-c(\boldsymbol{r})))\right].$$

We now introduce the reduced strain energy parameter, the reduced temperature and the reduced time as follows:

$$\kappa^*=|v(0)_{\rm f}-\kappa_0/8|^{-1}\kappa_0,\quad T^*=|v(0)_{\rm f}-\kappa_0/8|^{-1}K_BT,\quad t^*=|v(0)_{\rm f}-\kappa_0/8|^{-1}K_BT\lambda_1^{-1}t.$$

From (3.2) and (3.3), we obtain that

$$v(0)_{\rm f}=2\omega_1+\beta\omega_2=(2\gamma+\beta)\omega_2\leq 0, \tag{3.5}$$

which brings $|v(0)_{\rm f}-\kappa_0/8|=-(v(0)_{\rm f}-\kappa_0/8)$, and thus $\kappa_0/\kappa^*=-(v(0)_{\rm f}-\kappa_0/8)$. This leads to

$$\kappa_0=-\frac{8\kappa^*}{8-\kappa^*}v(0)_{\rm f}. \tag{3.6}$$

Consequently,

$$\left|v(0)_{\rm f}-\frac{\kappa_0}{8}\right|=-\left(v(0)_{\rm f}-\frac{\kappa_0}{8}\right)=-\frac{8}{8-\kappa^*}v(0)_{\rm f}. \tag{3.7}$$

Now let us denote

$$v^*(\boldsymbol{k})_{\rm f}=-\left(\frac{(8-\kappa^*)}{8(2\gamma+\beta)}\right)\Big(\gamma(\cos(k_xa)+\cos(k_ya))+\beta\cos(k_xa)\cos(k_ya)\Big).$$

From (3.2), (3.3) and (3.5), we see that

$$\begin{aligned} v(\boldsymbol{k})_{\rm f}&=\omega_2\Big(\gamma(\cos k_xa+\cos k_ya)+\beta\cos k_xa\cos k_ya\Big)\\ &=\frac{v(0)_{\rm f}}{2\gamma+\beta}\Big(\gamma(\cos k_xa+\cos k_ya)+\beta\cos k_xa\cos k_ya\Big)\\ &=\Big|v(0)_{\rm f}-\frac{\kappa_0}{8}\Big|\,v^*(\boldsymbol{k})_{\rm f}. \end{aligned}\tag{3.8}$$

Along with (3.6)-(3.7), this leads to

$$v(\boldsymbol{k})=v(\boldsymbol{k})_{\rm f}+\kappa_0\left(e_x^2e_y^2-\frac{1}{8}\right)=\Big|v(0)_{\rm f}-\frac{\kappa_0}{8}\Big|\left(v^*(\boldsymbol{k})_{\rm f}+\kappa^*\left(e_x^2e_y^2-\frac{1}{8}\right)\right).$$

Now the dimensionless form of the kinetic equation (2.2) is defined as: find $\eta(\boldsymbol{r},t^*)\in H^1(0,T_{\rm ime};C(\Omega))$ such that

$$\begin{cases} \dfrac{\partial\widetilde{\eta}(\boldsymbol{k},t^*)}{\partial t^*}=\widetilde{\lambda}^*(\boldsymbol{k})\Big\{\widetilde{G}^*_{T^*}(\eta(\boldsymbol{r},t^*))\Big\}_{\boldsymbol{k}}, \quad \boldsymbol{r}\in\Omega,\\ \widetilde{\eta}(\boldsymbol{r},0)=\widetilde{\eta}_0, \end{cases}\tag{3.9}$$

where

$$\widetilde{\lambda}^*(\boldsymbol{k})=-2\big(2-\cos(k_xa)-\cos(k_ya)\big),\tag{3.10}$$

and $\{\widetilde{G}^*_{T^*}(\eta(\boldsymbol{r},t^*))\}_{\boldsymbol{k}}$ is the Fourier transforms of the nonlinear function

$$G^*_{T^*}(\eta(\boldsymbol{r},t^*))=c(\boldsymbol{r})(1-c(\boldsymbol{r}))\frac{\delta\mathcal{F}^*_{\rm ree}}{\delta\eta(\boldsymbol{r},t^*)}.\tag{3.11}$$

In (3.11), $\mathcal{F}^*_{\rm ree}=|v(0)_{\rm f}-\kappa_0/8|^{-1}\mathcal{F}_{\rm ree}$ satisfies

$$\left\{\widetilde{\frac{\delta\mathcal{F}^*_{\rm ree}}{\delta\eta(\boldsymbol{r},t^*)}}\right\}_{\boldsymbol{k}}=\left(v^*(\boldsymbol{k})_{\rm f}+\kappa^*\left(e_x^2e_y^2-\frac{1}{8}\right)\right)\widetilde{\eta}(\boldsymbol{k},t^*)+T^*\left\{\widetilde{\phi}(\eta(\boldsymbol{r},t^*))\right\}_{\boldsymbol{k}}.\tag{3.12}$$

Remark 3.1. Eq. (3.9) can also be used to describe the phenomenon with discontinuous composition term. Let the curve $\Gamma=\overline{\Omega}_1\cap\overline{\Omega}_2$ ($\Omega=\Omega_1\cup\Omega_2\cup\Gamma$, $\Omega_1\cap\Omega_2=\phi$) and

$$c(\boldsymbol{r})=\begin{cases} c_1(\boldsymbol{r}), & \boldsymbol{r}\in\Omega_1,\\ c_2(\boldsymbol{r}), & \boldsymbol{r}\in\Omega_2. \end{cases}$$

Clearly, the function $c(\boldsymbol{r})$ is discontinuous on Γ if $c_1(\boldsymbol{r})\neq c_2(\boldsymbol{r})$. Then (3.9) is understood as

$$\begin{cases} \dfrac{\partial\widetilde{\eta}(\boldsymbol{k},t^*)}{\partial t^*}=\widetilde{\lambda}^*(\boldsymbol{k})\left\{\widetilde{G}^*_{T^*}(\eta(\boldsymbol{r},t^*))\right\}_{\boldsymbol{k}}, \quad \boldsymbol{r}\in\Omega, \\ \eta(\boldsymbol{r},t^*) \text{ is continuous on } \Gamma, \\ \widetilde{\eta}(\boldsymbol{r},0)=\widetilde{\eta}_0. \end{cases}$$

Remark 3.2. If the temperature function $T^*(t)$ is dependent on the time t and has a discontinuous at time t_1,

$$T^*(t)=\begin{cases} T_1^*, & 0<t\leq t_1, \\ T_2^*, & t_1<t\leq T_{\text{ime}}, \end{cases}$$

where $T_1^*\neq T_2^*$. Then (3.9) is understood as

$$\begin{cases} \dfrac{\partial\widetilde{\eta}(\boldsymbol{k},t^*)}{\partial t^*}=\widetilde{\lambda}^*(\boldsymbol{k})\left\{\widetilde{G}^*_{T_1^*}(\eta(\boldsymbol{r},t^*))\right\}_{\boldsymbol{k}}, \quad 0\leq t^*\leq t_1, \\ \dfrac{\partial\widetilde{\eta}(\boldsymbol{k},t^*)}{\partial t^*}=\widetilde{\lambda}^*(\boldsymbol{k})\left\{\widetilde{G}^*_{T_2^*}(\eta(\boldsymbol{r},t^*))\right\}_{\boldsymbol{k}}, \quad t_1<t^*\leq T_{\text{ime}}, \\ \widetilde{\eta}(\boldsymbol{k},t_1^-)=\widetilde{\eta}(\boldsymbol{k},t_1^+), \\ \widetilde{\eta}(\boldsymbol{r},0)=\widetilde{\eta}_0. \end{cases}$$

4 Time stepping methods

4.1 Classical scheme

Since (3.9) is a nonlinear equation with respect to $\tilde{\eta}(\boldsymbol{k},t^*)$, the numerical methods for solving it should be developed for dealing with the problems of practical significance. We consider a time-discrete framework associated to the time interval $I=]0,T_{\text{ime}}]$. We divide $\bar{I}=[0,T_{\text{ime}}]$ into $M_{\Delta t_f}$ subintervals of equal length $\Delta t_f=T_{\text{ime}}/M_{\Delta t_f}$ and denote

$$t^m_{\Delta t_f}=m\Delta t_f, \qquad 0\leq m\leq M_{\Delta t_f}\equiv T_{\text{ime}}/\Delta t_f,$$

and define

$$I_{\Delta t_f}\equiv\{0,1,\cdots,M_{\Delta t_f}\}.$$

The fine approximated propagator $\mathcal{F}_t$ is defined as: find $\eta^{m+1}\in C(\Omega)$ such that

$$\begin{cases} \tilde{\eta}^{m+1,[0]}(\boldsymbol{k})=\tilde{\eta}^m(\boldsymbol{k})+\Delta t_f\widetilde{\lambda}^*(\boldsymbol{k})\left\{\widetilde{G}^*_{T^*}(\eta^m)\right\}_{\boldsymbol{k}}, \\ \tilde{\eta}^{m+1,[n]}(\boldsymbol{k})=\tilde{\eta}^m(\boldsymbol{k})+\dfrac{1}{2}\Delta t_f\widetilde{\lambda}^*(\boldsymbol{k})\left(\left\{\widetilde{G}^*_{T^*}(\eta^m)\right\}_{\boldsymbol{k}}+\left\{\widetilde{G}^*_{T^*}(\eta^{m+1,[n-1]})\right\}_{\boldsymbol{k}}\right), \\ \qquad\qquad\qquad\qquad\qquad\qquad\qquad\qquad\qquad\qquad n=1,\cdots,n_0, \\ \tilde{\eta}^{m+1}(\boldsymbol{k})=\tilde{\eta}^{m+1,[n_0]}(\boldsymbol{k}), \quad m\in I_{\Delta t_f}, \\ \tilde{\eta}^0(\boldsymbol{k})=\tilde{\eta}_0(\boldsymbol{k}), \end{cases} \tag{4.1}$$

and the corresponding algorithm can be carried out by an offline-online procedure as follows:

Off-line Stage

In the offline stage, all of the following precomputing are performed only once.

(1). Calculate $\tilde{\eta}^0(\boldsymbol{k})$ and $\{\tilde{\phi}(\eta^0)\}_{\boldsymbol{k}}$.

(2). Evaluate and store $\widetilde{\lambda}^*(\boldsymbol{k})$, $v^*(\boldsymbol{k})_{\rm f}$, $\left(e_x^2e_y^2-\dfrac{1}{8}\right)$ and $c(\boldsymbol{r})(1-c(\boldsymbol{r}))$.

On-line Stage

Let $\eta^m(\boldsymbol{r})$ be given. In the online stage we need only do the following steps:

(1). Compute $\phi(\eta^m(\boldsymbol{k}))$ and $\{\widetilde{\phi}(\eta^m(\boldsymbol{k}))\}_{\boldsymbol{k}}$. Then use (3.12) to form

$$\left\{\widetilde{\frac{\delta\mathcal{F}_{\rm ree}^*}{\delta\eta}}(\eta^m(\boldsymbol{r}))\right\}_{\boldsymbol{k}}=\left(v^*(\boldsymbol{k})_{\rm f}+\kappa^*\left(e_x^2e_y^2-\frac{1}{8}\right)\right)\tilde{\eta}^m(\boldsymbol{k})+T^*\{\widetilde{\phi}(\eta^m(\boldsymbol{r}))\}_{\boldsymbol{k}};$$

(2). Evaluate $\frac{\delta\mathcal{F}_{\rm ree}^*}{\delta\eta}(\eta^m(\boldsymbol{r}))$ and use (3.11) to form

$$G_{T^*}^*(\eta^m(\boldsymbol{r}))=c(\boldsymbol{r})(1-c(\boldsymbol{r}))\frac{\delta\mathcal{F}_{\rm ree}^*}{\delta\eta}(\eta^m(\boldsymbol{r}));$$

(3). Calculate $\{\widetilde{G^*}_{T^*}(\eta^m(\boldsymbol{r}))\}_{\boldsymbol{k}}$ to obtain $\tilde{\eta}^{m+1,[0]}(\boldsymbol{k})$ by the first scheme of (4.1);

Assume $\eta^{m+1,[n-1]}(\boldsymbol{k})$ is known for each $1\le n\le n_0-1$.

(4). Repeat the above procedure (1)-(3) to obtain

$$\begin{aligned}&\phi(\eta^{m+1,[n-1]}(\boldsymbol{k}))\Rightarrow\left\{\widetilde{\phi}(\eta^{m+1,[n-1]}(\boldsymbol{k}))\right\}_{\boldsymbol{k}}\Rightarrow\left\{\widetilde{\frac{\delta\mathcal{F}_{\rm ree}^*}{\delta\eta}}(\eta^{m+1,[n-1]}(\boldsymbol{r}))\right\}_{\boldsymbol{k}}\\ \Rightarrow\ &\frac{\delta\mathcal{F}_{\rm ree}^*}{\delta\eta}(\eta^{m+1,[n-1]}(\boldsymbol{r}))\Rightarrow G_{T^*}^*(\eta^{m+1,[n-1]}(\boldsymbol{r}))\Rightarrow\left\{\widetilde{G^*}_{T^*}(\eta^{m+1,[n-1]}(\boldsymbol{r}))\right\}_{\boldsymbol{k}}.\end{aligned}$$

Then $\tilde{\eta}^{m+1,[n]}(\boldsymbol{k})$ follows from the second scheme of (4.1).

It is well known that the semi-implicit treatment in time allows a consistently large time-step size. Usually, the time-step in a semi-implicit method can be two orders of magnitude larger than that in an explicit method [17, 22, 23]. We consider the semi-implicity method for (3.9) if the composition $c(\boldsymbol{r})=c$ is a constant. Let us denote

$$\begin{aligned}A(\boldsymbol{k})&=\Delta t_f c(1-c)\widetilde{\lambda}^*(\boldsymbol{k})\left(v^*(\boldsymbol{k})_{\rm f}+\kappa^*\left(e_x^2e_y^2-\frac{1}{8}\right)\right),\\ B(\boldsymbol{k})&=\Delta t_f c(1-c)\widetilde{\lambda}^*(\boldsymbol{k})T^*.\end{aligned}$$

Then the second-order semi-implicity Runge-Kutta (SIRK2) scheme is as follows:

$$\begin{cases} \tilde{\eta}^{m+1}_{\text{pre}}(\boldsymbol{k}) = \tilde{\eta}^{m}(\boldsymbol{k}) + \dfrac{1}{2}A(\boldsymbol{k})\left(\tilde{\eta}^{m+1}_{\text{pre}}(\boldsymbol{k}) + \tilde{\eta}^{m}(\boldsymbol{k})\right) + B(\boldsymbol{k})\left\{\tilde{\phi}(\eta^{m}(\boldsymbol{r}))\right\}_{\boldsymbol{k}}, \\ \tilde{\eta}^{m+1}(\boldsymbol{k}) = \tilde{\eta}^{m}(\boldsymbol{k}) + \dfrac{1}{2}A(\boldsymbol{k})\left(\tilde{\eta}^{m+1}(\boldsymbol{k}) + \tilde{\eta}^{m}(\boldsymbol{k})\right) \\ \qquad\qquad + \dfrac{1}{2}B(\boldsymbol{k})\left(\left\{\tilde{\phi}(\eta^{m+1}_{\text{pre}}(\boldsymbol{r}))\right\}_{\boldsymbol{k}} + \left\{\tilde{\phi}(\eta^{m}(\boldsymbol{r}))\right\}_{\boldsymbol{k}}\right), \\ \tilde{\eta}^{0}(\boldsymbol{k}) = \tilde{\eta}_0(\boldsymbol{k}). \end{cases}$$

Also, the corresponding offline-online procedure can be carried out:

Off-line Stage

1. Calculate $\tilde{\eta}^0(\boldsymbol{k})$ and $\left\{\tilde{\phi}(\eta^0)\right\}_{\boldsymbol{k}}$.
2. Evaluate and store $A(\boldsymbol{k})$, $A_0(\boldsymbol{k})$ and $B_0(\boldsymbol{k})$, where

$$A_0(\boldsymbol{k}) = \left[1 - \frac{1}{2}A(\boldsymbol{k})\right]^{-1}\left[1 + \frac{1}{2}A(\boldsymbol{k})\right], \tag{4.2a}$$

$$B_0(\boldsymbol{k}) = \left[1 - \frac{1}{2}A(\boldsymbol{k})\right]^{-1}B(\boldsymbol{k}). \tag{4.2b}$$

On-line Stage

We need only compute

$$\begin{cases} \tilde{\eta}^{m+1}_{\text{pre}}(\boldsymbol{k}) = A_0(\boldsymbol{k})\tilde{\eta}^{m}(\boldsymbol{k}) + B_0(\boldsymbol{k})\left\{\tilde{\phi}(\eta^{m}(\boldsymbol{r}))\right\}_{\boldsymbol{k}}, \\ \tilde{\eta}^{m+1}(\boldsymbol{k}) = A_0(\boldsymbol{k})\tilde{\eta}^{m}(\boldsymbol{k}) + \dfrac{1}{2}B_0(\boldsymbol{k})\left(\left\{\tilde{\phi}(\eta^{m+1}_{\text{pre}}(\boldsymbol{r}))\right\}_{\boldsymbol{k}} + \left\{\tilde{\phi}(\eta^{m}(\boldsymbol{r}))\right\}_{\boldsymbol{k}}\right). \end{cases} \tag{4.3}$$

So we share the advantage of the explicit scheme.

4.2 Multi-model Euler scheme

Let us divide $\bar{I}$ into $M_{\Delta t_c}$ subintervals of equal length $\Delta t_c = T_{\text{ime}}/M_{\Delta t_c}$ and denote

$$t^k_{\Delta t_c} = k\Delta t_c, \qquad 0 \le k \le M_{\Delta t_c} \equiv T_{\text{ime}}/\Delta t_c,$$

and define

$$I_{\Delta t_c} \equiv \{0, 1, \cdots, M_{\Delta t_c}\}.$$

By the Taylor's expansion, we have

$$\ln x = 2\left\{\frac{x-1}{x+1} + \frac{1}{3}\left(\frac{x-1}{x+1}\right)^3 + \frac{1}{5}\left(\frac{x-1}{x+1}\right)^5 + \cdots\right\}, \quad x > 0 \tag{4.4}$$

which brings

$$\ln\frac{\eta}{1-\eta}\approx 2(2\eta-1)\left(1+\frac{1}{3}(2\eta-1)^2\right)=\psi(\eta(\boldsymbol{r},t^*).$$

We consider another model of (3.9): find $\tilde{\eta}(\boldsymbol{k},t^*)$ such that

$$\begin{cases}\dfrac{\partial\widetilde{\eta}(\boldsymbol{k},t^*)}{\partial t^*}=\widetilde{\lambda}^*(\boldsymbol{k})\left\{\widetilde{H}^*_{T^*}(\eta(\boldsymbol{r},t^*))\right\}_{\boldsymbol{k}},\\ \widetilde{\eta}(\boldsymbol{r},0)=\widetilde{\eta}_0,\end{cases}\tag{4.5}$$

where $\{\widetilde{H}^*_{T^*}(\eta(\boldsymbol{r},t^*))\}_{\boldsymbol{k}}$ is the Fourier transforms of the nonlinear function

$$H^*_{T^*}(\eta(\boldsymbol{r},t^*))=c(\boldsymbol{r})(1-c(\boldsymbol{r}))\frac{\delta\mathsf{F}^*_{\text{ree}}}{\delta\eta(\boldsymbol{r},t^*)}.\tag{4.6}$$

It can be verified that

$$\left\{\widetilde{\frac{\delta\mathsf{F}^*_{\text{ree}}}{\delta\eta(\boldsymbol{r},t^*)}}\right\}_{\boldsymbol{k}}=\left(v^*(\boldsymbol{k})_{\text{f}}+\kappa^*\left(e_x^2e_y^2-\frac{1}{8}\right)\right)\widetilde{\eta}(\boldsymbol{k},t^*)+T^*(t^*)\left\{\widetilde{\psi}(\eta(\boldsymbol{r},t^*))\right\}_{\boldsymbol{k}}.\tag{4.7}$$

We point out here, the nonlinear term $\left\{\widetilde{\psi}(\eta(\boldsymbol{r},t^*)\right\}_{\boldsymbol{k}}$ can be evaluated by using the Orszag's transform method. The multi-model Euler (MME) scheme: find $\eta^{k+1}\in C(\Omega)$ such that

$$\begin{cases}\tilde{\eta}^{k+1}_{\text{pre}}(\boldsymbol{k})=\tilde{\eta}^k(\boldsymbol{k})+\Delta t_c\widetilde{\lambda}^*(\boldsymbol{k})\left\{\widetilde{H}^*_{T^*}(\eta^k)\right\}_{\boldsymbol{k}},\\ \tilde{\eta}^{k+1}(\boldsymbol{k})=\tilde{\eta}^k(\boldsymbol{k})+\Delta t_c\widetilde{\lambda}^*(\boldsymbol{k})\left\{\widetilde{G}^*_{T^*}(\eta^{k+1}_{\text{pre}})\right\}_{\boldsymbol{k}},\quad k\in I_{\Delta t_c},\\ \tilde{\eta}^0(\boldsymbol{k})=\tilde{\eta}_0(\boldsymbol{k}).\end{cases}\tag{4.8}$$

Thus the MME scheme is fast and inexpensive.

4.3 Numerical simulations and variable temperature schemes

In this section some results of the simulations using the scheme (4.1) with $N=128$ are shown. A 128×128 Fourier modes has been used on the square $[0,128]\times[0,128]$. The morphological evolution from the "as-quenched" state of the system which is determined by an initial condition

$$\eta(\boldsymbol{r},0)=c_0+\delta c_0(\boldsymbol{r}),\tag{4.9}$$

where c_0 is the average composition of the solution and $\delta c_0(\boldsymbol{r})$ is a random perturbation with values distributed uniformly between $+0.01$ and -0.01.

Example 4.1. Consider Eq. (3.9) with $T^*=0.095$, $\gamma=100$, $\beta=20$, $\kappa^*=1.25$, and the composition function

$$c(\boldsymbol{r})=c+K(T^*)\xi(\boldsymbol{r}),\tag{4.10}$$

where the constant $c=0.25$, $K(T^*)=4(T^*)^2$ and $\xi(\boldsymbol{r})$ is a random noise with values distributed uniformly between 0 and 1.

In Fig. 1, we presented the temporal evolution of morphological patterns which undergoing asymmetrical spinodal decomposition and subsequent coarsening with the elastic strain effect. Various shades of grey represent different values of occupation probability of solution atoms in which completely red represents a value of one while completely blue represents a value of zero. The simulations show that initial compositions which are perturbations of a uniform state in the spinodal interval ($c_0=0.3$) evolve rapid into a phase separated structure. After this rapid evolution a slow coarsening process takes place involving an increase of the size of the phase domains.

When a significant lattice mismatch between the two product phases is assumed, an anisotropic structure composed of alternative $\{01\}$ thin strips of the two product phases is obtained, the larger the value of κ, the stronger the anisotropy of the structure formed (see Fig. 1). In the early stage of decomposition, only concentration waves along the elastically soft directions develop (see Fig.1). Superposition of these waves while they grow towards their equilibrium amplitudes generates an interesting intermediate structure which looks like a "basket weave". It consists of solute-rich red strips and solute-lean blue strips weaving together along the soft direction. This morphology is agreement with the experimental observations by de Vos in ALNICO alloy [8], Butler and Thomas [4], Livak and Thomas [20] in Cu-Ni-Fe, Huang et al. [25] in Ni-Al-Fe, and Higgins et al. [21] in Fe-Be.

Example 4.2. Let $\Omega=(0,2\pi)^2$, $T^*=0.095$, $\gamma=100$, $\beta=20$, $\kappa^*=0$. Consider Eq. (3.9) with a discontinuous composition function

$$c(\boldsymbol{r})=\begin{cases} 0.5, & (x-\pi)^2+(y-\pi)^2\leq(36a)^2, \\ 0.25, & \text{others}, \end{cases} \tag{4.11}$$

where a is the crystal lattice parameter of a solid solution.

The initial condition is an "as-quenched" homogeneous cubic phase that is in a metastable state ($c_0=0.35$). Since no other crystal defects were considered, the transformation developed through a homogeneous nucleation process simulated by the random force driven. No a priori assumptions about possible critical nucleus configurations were made. The simulation result presented in Fig. 2(a) shows that the stochastic random noises produce critical nuclei along the discontinuous curve

$$\Gamma:\ (x-\pi)^2+(y-\pi)^2=(36a)^2.$$

These nuclei were then formed by a collective process. Such an internally cubic structure of the embryos reduces considerably the strain energy. The growth process of the nuclei is obvious. It first appears in the interior of the curve Γ, and then diffuses to the domain.

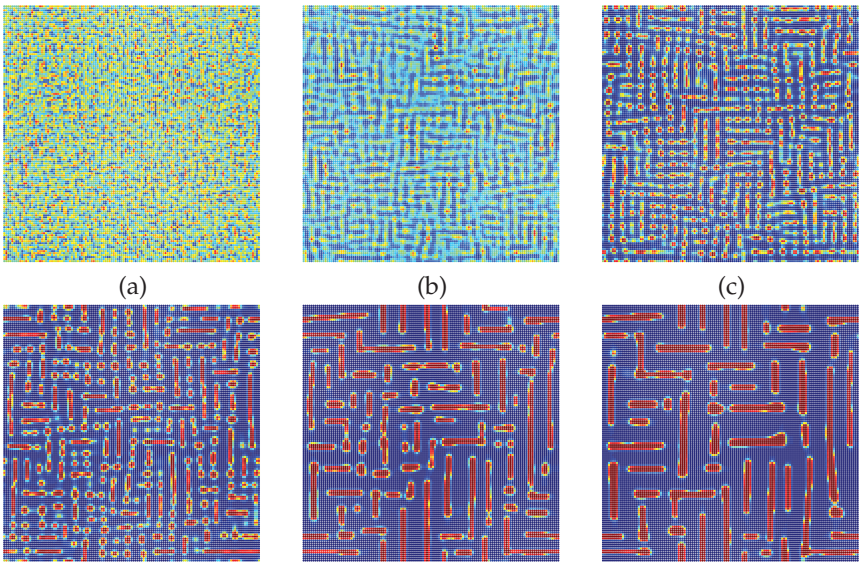

Figure 1: Temporal morphological evolutions of Example 4.1 with $\Delta t_f = 0.001$ at different time :(a) $t = 10$; (b) $t = 50$; (c) $t = 100$; (d) $t = 200$; (e) $t = 500$; (f) $t = 1000$.

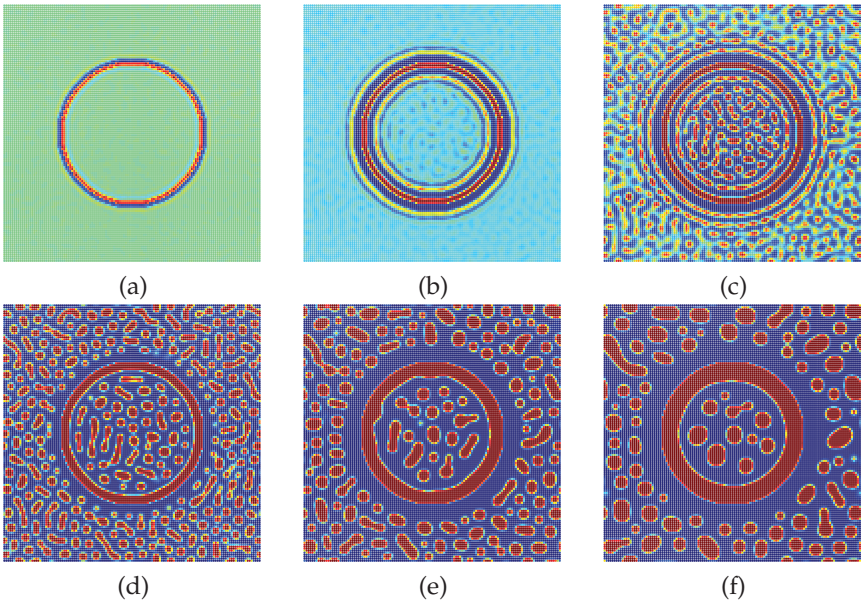

Figure 2: Temporal morphological evolutions of Example 4.2 with $\Delta t_f = 0.0001$ at different time :(a) $t = 10$; (b) $t = 50$; (c) $t = 100$; (d) $t = 200$; (e) $t = 500$; (f)$t = 1000$.

Example 4.3. Let $\gamma=100$, $\beta=20$, $\kappa^*=0$, and the composition function $c(\boldsymbol{r})=0.3$. Consider Eq. (3.9) with the following temperature function

$$T^*(t)=\begin{cases}0.095, & 0<t\leq 1000;\\ 0.075, & 1000<t\leq 1010;\\ 0.055, & 1010<t\leq 1020;\\ 0.035, & 1020<t\leq 1030;\\ 0.015, & 1030<t\leq 1040;\\ 0.0055, & 1040<t\leq 1100.\end{cases}$$

We try consider the numerical simulation at very low temperature. To this end, we first drive Eq. (3.9) at higher temperature $T^*=0.095$ for $0<t\leq 1000$. It is easy to know that the initial compositions ($c_0=0.32$) evolve rapid into a phase separated structure. Now we reduce the temperature from $T^*=0.095$ to $T^*=0.075$, and then to $T^*=0.055$ such that the function $\eta(\boldsymbol{r},t)$ approaches 1 or 0. Next, we introduce the term

$$\psi_m(\eta(\boldsymbol{r},t^*)=2(2\eta-1)\left(1+\frac{1}{3}(2\eta-1)^2+\frac{1}{5}(2\eta-1)^4+\cdots+\frac{1}{2m+1}(2\eta-1)^{2m}\right).$$

Using the formula

$$\sum_{k=1}^{n}\frac{1}{k}=\ln n+\gamma,\quad \gamma=0.5772,$$

we find that

$$\lim_{\eta\to 1}\psi_m(\eta(\boldsymbol{r},t^*)=2\left(\sum_{k=1}^{2m+1}\frac{1}{k}-\sum_{k=1}^{m}\frac{1}{2k}\right)=\ln\left(4m+4+\frac{1}{m}\right)+\gamma.$$

Hence

$$\lim_{\eta\to 1}\ln\frac{\eta}{1-\eta}=\lim_{m\to\infty}\ln\left(4m+4+\frac{1}{m}\right)+\gamma,$$

which, a priori, prevents from the very low temperature simulations.

Now let $\{\widetilde{H}^m_{T^*}(\eta(\boldsymbol{r},t^*))\}_{\boldsymbol{k}}$ be the Fourier transforms of the nonlinear function

$$H^m_{T^*}(\eta(\boldsymbol{r},t^*))=c(\boldsymbol{r})(1-c(\boldsymbol{r}))\frac{\delta \mathsf{F}^*_{\text{ree}}}{\delta\eta(\boldsymbol{r},t^*)},$$

in which

$$\left\{\widetilde{\frac{\delta \mathsf{F}^*_{\text{ree}}}{\delta\eta(\boldsymbol{r},t^*)}}\right\}_{\boldsymbol{k}}=\left(v^*(\boldsymbol{k})_{\text{f}}+\kappa^*\left(e_x^2e_y^2-\frac{1}{8}\right)\right)\widetilde{\eta}(\boldsymbol{k},t^*)+T^*(t^*)\left\{\widetilde{\psi}_m(\eta(\boldsymbol{r},t^*))\right\}_{\boldsymbol{k}}.$$

The very low temperature model and the corresponding variable temperature explicit Euler scheme reads as follows:

$$\begin{cases} \tilde{\eta}^{n+1}(\boldsymbol{k})=\tilde{\eta}^{n}(\boldsymbol{k})+\Delta t_f\widetilde{\lambda}^{*}(\boldsymbol{k})\left\{\widetilde{H}^{m}_{0.0055}(\eta^n)\right\}_{\boldsymbol{k}}, & 1040<t\leq 1100,\\ \tilde{\eta}(\boldsymbol{k},1040^{-})=\tilde{\eta}(\boldsymbol{k},1040^{+}),\\ \tilde{\eta}^{n+1}(\boldsymbol{k})=\tilde{\eta}^{n}(\boldsymbol{k})+\Delta t_f\widetilde{\lambda}^{*}(\boldsymbol{k})\left\{\widetilde{H}^{m}_{0.015}(\eta^n)\right\}_{\boldsymbol{k}}, & 1030<t\leq 1040,\\ \tilde{\eta}(\boldsymbol{k},1030^{-})=\tilde{\eta}(\boldsymbol{k},1030^{+}),\\ \tilde{\eta}^{n+1}(\boldsymbol{k})=\tilde{\eta}^{n}(\boldsymbol{k})+\Delta t_f\widetilde{\lambda}^{*}(\boldsymbol{k})\left\{\widetilde{H}^{m}_{0.035}(\eta^n)\right\}_{\boldsymbol{k}}, & 1020<t\leq 1030,\\ \tilde{\eta}(\boldsymbol{k},1020^{-})=\tilde{\eta}(\boldsymbol{k},1020^{+}),\\ \tilde{\eta}^{n+1}(\boldsymbol{k})=\tilde{\eta}^{n}(\boldsymbol{k})+\Delta t_f\widetilde{\lambda}^{*}(\boldsymbol{k})\left\{\widetilde{G}^{*}_{0.055}(\eta^n)\right\}_{\boldsymbol{k}}, & 1010<t\leq 1020,\\ \tilde{\eta}(\boldsymbol{k},1010^{-})=\tilde{\eta}(\boldsymbol{k},1010^{+}),\\ \tilde{\eta}^{n+1}(\boldsymbol{k})=\tilde{\eta}^{n}(\boldsymbol{k})+\Delta t_f\widetilde{\lambda}^{*}(\boldsymbol{k})\left\{\widetilde{G}^{*}_{0.075}(\eta^n)\right\}_{\boldsymbol{k}}, & 1000<t\leq 1010,\\ \tilde{\eta}(\boldsymbol{k},1000^{-})=\tilde{\eta}(\boldsymbol{k},1000^{+}),\\ \tilde{\eta}^{n+1}(\boldsymbol{k})=\tilde{\eta}^{n}(\boldsymbol{k})+\Delta t_f\widetilde{\lambda}^{*}(\boldsymbol{k})\left\{\widetilde{G}^{*}_{0.095}(\eta^n)\right\}_{\boldsymbol{k}}, & 0<t\leq 1000,\\ \tilde{\eta}^{0}(\boldsymbol{k})=\tilde{\eta}_0(\boldsymbol{k}). \end{cases} \tag{4.12}$$

The other time stepping schemes can be carried out similarly. In our simulations, we use the second-order Runge-Kutta scheme. Some microstructures with the very low tem-

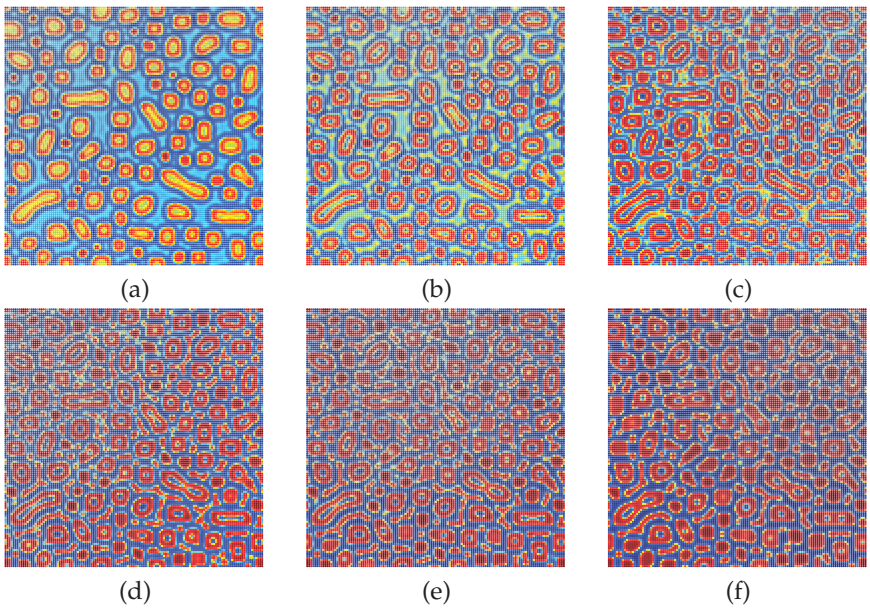

Figure 3: Very low temperature microstructure characteristic of Example 4.3 with $\Delta t_f=0.0001$ at different time: (a) $t=1030$; (b) $t=1040$; (c) $t=1050$; (d) $t=1060$; (e) $t=1070$; (f) $t=1100$.

perature characteristic are obtained. The simulation results for $m=3$ are presented in Fig. 3.

5 Parallel in time discretization

Finding efficient algorithms to solve the kinetic equation (3.9) is a first step towards simulating morphological transformation in cubic alloys. But, however fast these algorithms may be, the need for solving evolution equation is still present and is very time consuming. One of the approaches to lower the total time required in order to solve this equation may be to take advantage of the parallel computing architectures available nowadays.

5.1 Parareal in time algorithm

The parareal in time algorithm allows to use parallel computers for the approximation of the solution to ordinary or evolution partial differential equations by decomposing the time integration interval into time slabs and iterating on the resolution over each time slab to converge to the global solution. The iterations combine in a predictor/corrector way the use of a coarse propagator that is inexpensive and a precise solver (that is used only in parallel over each time slab, allocated to different processors). In many instances the iterative schemes provide an approximate solution as accurate as if the precise solver would be used over the complete time integration interval, such as the parareal in time molecular dynamics simulation, the parareal time discretization of the pricing of American Put and the parareal control of quantum systems; see, e.g., [1,2,24,26,29]. Let

$$0=t_0<t_1<\cdots<t_n=n\Delta t<\cdots<t_M=T_{\text{ime}}$$

be special times at which we are interested to consider snapshots of the solution $\eta(\boldsymbol{r},t_n)$, then we introduce a fine and precise approximated propagator $\mathcal{F}_t$ defined by (4.1). Thus we obtain that the approximations η^n of $\eta(\boldsymbol{r},t_n)$ given by

$$\eta^{n+1}=\mathcal{F}_{t_{n+1}}(\eta^0)=\mathcal{F}_{t_{n+1}-t_n}(\eta^n).$$

Assuming, for the sake of simplicity, that $t_{n+1}-t_n$ is constant Δt ($\Delta t >> \Delta t_f$), then this reads

$$\eta^{n+1}=\mathcal{F}_{\Delta t}(\eta^n), \tag{5.1}$$

where it appears that the approximated solution process is sequential, which, a priori, prevents from a parallelization.

In what follows Lions et al. [19] proposed an algorithm $\eta_j^n \longrightarrow \eta^n$ as j goes to infinity. For this we employ another coarse propagator $\mathcal{G}_t$ defined by (4.8). Then, the iterative process now reads as follows:

$$\eta_{j+1}^{n+1}=\mathcal{G}_{\Delta t}(\eta_{j+1}^n)+\mathcal{F}_{\Delta t}(\eta_j^n)-\mathcal{G}_{\Delta t}(\eta_j^n). \tag{5.2}$$

In summary, the parareal in time algorithm for (3.9) consists of the following steps:

(1) Initialization: compute $\eta_1^{n+1}=\mathcal{G}_{\Delta t}(\eta_1^n)$ (sequential);

Assume $\{\eta_j^n\}_{n=1,2,\cdots,M}$ is known at step j.

(2) Resolution over each $]t_n,t_{n+1}[$: $\mathcal{F}_{\Delta t}(\eta_j^n)$ (parallel);

(3) Correction at each initial time t_n using (5.2) (sequential);

(4) until convergence.

5.2 The convergence

We shall test the convergence and show the accuracy of the iterative process (5.2) for the different parallel time step Δt. Define the relative error as

$$E^j(\eta(\mathbf{r},t_n^*))=\frac{\|\eta(t_n^*)-\eta_j^n\|_{L^\infty(\Omega)}}{\|\eta(t_n^*)\|_{L^\infty(\Omega)}}.$$

Example 5.1. Take $\Delta t_f=0.001$ and $\Delta t_c=0.01$. Consider the parareal in time simulation of Example 4.1 with $c_0=0.45$ on the time interval $(0,T_{\text{ime}}]$ where $T_{\text{ime}}=1000$.

The numerical results of $E^j(\eta(\boldsymbol{r},1000))$ for Example 5.1 is presented in Table 1. It indicates that the iterative process (5.2) is nearly unconditionally convergent for Δt. So our parareal in time algorithm can be performed on every kind of parallel computer, and thus we match the computational efficiency with the computer well. Indeed, we know from (5.2) that the error

$$\|\eta^n-\eta_j^n\|_{L^\infty(\Omega)}\leq\|\eta^n-\eta(\mathbf{r},t_n^*)\|_{L^\infty(\Omega)}+\|\eta(\mathbf{r},t_n^*)-\eta_j^n\|_{L^\infty(\Omega)}\approx\Delta t_f^2+\varepsilon^j(\Delta t).$$

Hence, if we use the iterative scheme (5.2) with j=2, the accuracy of Example 5.1 arrives at $\mathcal{O}(\Delta t_f^2)\approx\mathcal{O}(10^{-6})$. In Fig. 4, we show the relative errors of Example 5.1 at 250 snapshots of the solution $\eta(\boldsymbol{r},t_n)$. It indicates that the iterative process (5.2) is convergent at $j=4$. Indeed, the error curve $j=4$ is coincide with the $j=5$ one.

Table 1: The relative error $E^j(\eta(\boldsymbol{r},1000))$ of Example 5.1.

j	$\Delta t=1$	$\Delta t=2$	$\Delta t=4$	$\Delta t=8$	$\Delta t=16$
1	2.79E-4	2.00E-3	1.10E-3	3.12E-5	2.13E-4
2	4.02E-6	4.02E-6	2.24E-6	1.94E-7	3.36E-7
3	6.94E-8	5.46E-8	1.43E-8	8.52E-10	5.55E-10
4	1.01E-9	2.13E-10	5.61E-11	7.45E-12	1.39E-12
5	1.25E-11	3.58E-11	5.72E-11	4.48E-12	5.48E-13

Example 5.2. Take $\Delta t_f=0.0001$ and $\Delta t_c=0.01$. Consider the parareal in time simulation of Example 4.2 with $c_0=0.32$ on the time interval $(0,T_{\text{ime}}]$ where $T_{\text{ime}}=1000$.

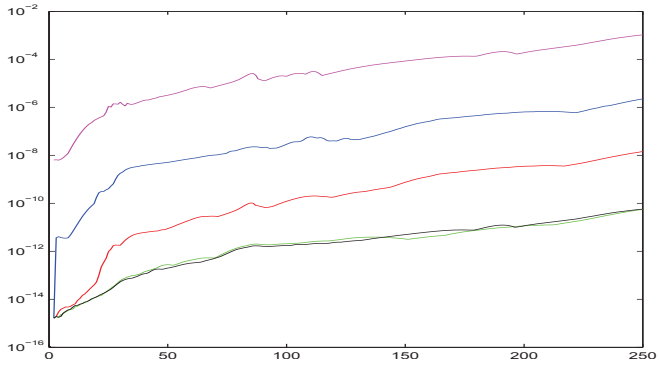

Figure 4: The convergence of Example 5.1 with $\Delta t=4$ under the iterative number $j=1$ (cyan), $j=2$ (blue), $j=3$ (red), $j=4$ (green) and $j=5$ (black).

The numerical results of $E^j(\eta(\boldsymbol{r},1000))$ for Example 5.2 are presented in Table 2. Again, it indicates that the iterative process (5.2) is nearly unconditionally convergent for Δt. If we use the iterative process (5.2) with $j=3$, the accuracy of Example 5.2 arrives at $\mathcal{O}(\Delta t_f^2)\approx\mathcal{O}(10^{-8})$. Hence, this is an efficient parallel time algorithm for the longer-term simulation.

Table 2: The relative error $E^j(\eta(\boldsymbol{r},1000))$ of Example 5.2.

j	$\Delta t=1$	$\Delta t=2$	$\Delta t=4$	$\Delta t=8$	$\Delta t=16$
1	3.24E-4	6.19E-4	8.66E-4	4.56E-4	1.51E-4
2	1.02E-5	9.82E-6	6.15E-6	3.65E-6	9.86E-7
3	2.85E-7	6.67E-8	3.38E-8	1.98E-8	3.62E-9
4	6.38E-9	7.92E-10	4.41E-10	1.02E-10	1.12E-11
5	1.31E-10	2.93E-11	2.40E-11	3.63E-12	2.04E-12

6 Conclusions

In this paper, we have presented the variable temperature schemes, the multi-model schemes and the parareal in time simulation for the reduced model of strain-induced morphological transformation in cubic binary alloys. We have demonstrated that a fixed algorithmic time step driving scheme may provide high accuracy and stability, and a coarse solver based on multi-model schemes can provide high accuracy and significant speedup for longer-term simulation. The parareal in time algorithm presented in this paper has satisfying efficiency for computing the solutions of the ordinary and partial differential equations, which also provides a way to construct parallel time method. Although our variable temperature schemes and multi-model schemes improve the algorithmic accuracy and stability, it is noted that large algorithmic time steps may yield inaccuracies.

This saturation in the speedup results from the details of how the system's energy evolution (and its corresponding microstructural evolution) is governed by the effective time step.

It is expected that the variable temperature schemes and multi-model schemes proposed in this work may have extensive applications in a wide class of strain-induced systems. For example, it can be applied to the model of martensitic transformations. This method should allow researchers to improve the computational efficiency and accuracy associated with modeling the dynamics of materials systems. On the other hand, the present methodology developed in this paper is certainly limited to the dynamical model of transport that only has a first-order of time derivative of the order parameter. It would certainly be interesting to attempt to extend this methodology to the dynamics of phase transitions that contain higher-order term, such as those that violate the assumption of local equilibrium. Theoretical analysis of the variable temperature scheme and multi-model scheme in two-dimensional reciprocal space of strain-induced systems also seems challenging.

Acknowledgments

We wish to express our gratitude to the referees for their valuable suggestions. This research was supported by the National Natural Science Foundation of China (Grant No. 11171218) and the Special Foundation of Shanghai Jiaotong University for Science and Technology Innovation (Grant No. AE0710004).

References

[1] L. Baffico, S. Bernard, Y. Maday, G. Turinici and G. Zérah. Parallel in time molecular dynamics simulations. Phys. Rev. E, 66:057701-057706, 2002.
[2] G. Bal and Y. Maday. A "parareal" time discretization for non-linear PDE's with application to the pricing of an American Put, in: Recent developments in domain decomposition methods (Zürich, 2001), Vol. 23 of Lect. Notes Comput. Sci. Eng., Springer, Berlin, 2002.
[3] J.W. Barrett, J.F. Blowey and H. Garcke. On fully practical finite element approximations of degenerate Cahn-Hilliard systems. M2AN Math. Model. Numer. Anal., 35:713-748, 2001.
[4] E.P. Butler and G. Thomas. Structure and properties of spinodally decomposed Cu-Ni-Fe alloys. ACta Metall., 18:347-365, 1970.
[5] L.Q. Chen and J. Shen. Application of semi-implicit Fourier-spectral method to phase field equations. Comput. Phys. Comm., 108:147-158, 1998.
[6] M. Cheng and J.A. Warren. An efficient algorithm for solving the phase field crystal model. J. Comput. Phys., 227:6241-6248, 2008.
[7] M.I.M. Copetti and C.M. Elliot. Kinetics of phase decomposition processes: Numerical solutions to Cahn-Hilliard equation. Mater. Sci. and Technol., 6:273-283, 1990.
[8] K.J. De Vos. Microstructure of alnico alloys. J. Appl. Phys., 37:1100-1100, 1966.
[9] C.M. Elliot and D.A. French. Numerical studies of the Cahn-Hilliard equation for phase separation. IMA J. Appl. Math., 38:97-128, 1987.

[10] C.M. Elliot and D.A. French. A nonconforming finite element method for the two dimensional Cahn-Hilliard equation. SIAM J. Numer Anal., 26:884-903, 1989.
[11] C.M. Elliot, D.A. French and D.A. Milner. A second order splitting method for the Cahn-Hilliard equation. Numer. Math., 54:575-590, 1989.
[12] C.M. Elliot and S. Larsson. Error estimates with smooth and nonsmooth data for a finite element method for the Cahn-Hilliard equation for phase separation. Math. Comp., 58:603-630, 1992.
[13] D.J. Eyre. In: Computational and Mathematical Models of Microstructural Evolution, edited by J.W.Bullard et al. (Materials Research Society, Warrendale, PA, 1998), 39-46.
[14] D.J. Eyre. `http://www.math.utah.edu/ eyre/research/methods/stable.ps`
[15] X.B. Feng and A.Prohl. Error analysis of a mixed finite element method for the Cahn-Hilliard equation. Numer. Math., 99:47-84, 2004.
[16] D. Furihata. A stable and conservative finite difference scheme for the Cahn-Hilliard equation. Numer. Math., 87:675-699, 2001.
[17] Y.N. He, Y.X. Liu and T. Tang. On large time-stepping methods for the Cahn-Hilliard equation. Appl. Numer. Math., 57:616-628, 2007.
[18] A.G. Khachaturyan. Theory of Structural Transformations in Solids. Wiley, New York, 1983.
[19] J.-L. Loins, Y. Maday and G. Turinici. A parareal in time discretization of pde's. C.R. Acad. Sci. Paris, Serie I, 332:661-668, 2001.
[20] R.J. Livak and G. Thomas. Spinodally decomposed Cu-Ni-Fe alloys of asymetrical compositions. Acta Metall., 19:497-505, 1971.
[21] J. Higgins, R.B. Nicholson and P. Wilkes. Precipitation in the Fe-Be System. Acta Metall., 22:201-217, 1974.
[22] L.-P. He and Y.X. Liu. A class of stable spectral methods for the Cahn-Hilliard equation. J. Comput. Phys., 228:5101-5110, 2009.
[23] L.-P. He. Error estimation of a class of stable spectral approximation to the Cahn-Hilliard equation. J. Sci. Comput., 41:461-482, 2009.
[24] L.-P. He. The reduced basis technique as a coarse solver for parareal in time simulations. J. Comput. Math., 28:676-692, 2010.
[25] S.C. Huang, R.D. Field and D.D. Krueger. Microscopy and tensile behavior of melt-spun Ni-Al-Fe alloys. Metall. Mater. Trans. A, 21:959-970, 1990.
[26] Y. Maday. The parareal in time algorithm: application to quantum control and muiti-model simulation. SIAM conference, 2004.
[27] Y. Ni, L.H. He and L. Yin. Three-dimensional phase field modeling of phase separation in strained alloys. Mater. Chemi. and Phys., 78:442-447, 2003.
[28] R. Poduri and L.Q. Chen. Computer simulation of morphological evolution and coarsening kinetics of δ' (Al_3Li) precipitates in Al-Li alloys. Acta Mater., 46:3915-3928, 1998.
[29] Y. Maday, J. Salomon and G. Turinici. Monotonic parareal control for quantum systems. SIAM J. Numer. Anal., 45:2468-2482, 2007.
[30] D.J. Seol, S.Y. Hu, Y.L. Li, J. Shen, K.H. Oh and L.Q. Chen. Computer simulation of spinodal decomposition in constrained films. Acta Mater., 51:5173-5185, 2003.
[31] T.P. Schulze and P. Smereka. Simulation of three-dimensional strained heteroepitaxial growth using kinetic Monte Carlo. Commun. Comput. Phys., 10:1089-1112, 2011.
[32] C. Shen, J.P. Simmons and Y. Wang. Effect of elastic interaction on nucleation: I. Calculation of the strain energy of nucleus formation in an elastically anisotropic crystal of arbitrary microstructure. Acta Mater., 54:5617-5630, 2006.
[33] C. Shen, J.P. Simmons and Y. Wang. Effect of elastic interaction on nucleation: II. Imple-

mentation of strain energy of nucleus formation in the phase field method. Acta Mater., 55:1457-1466, 2007.
[34] B.P. Vollmayr-Lee and A.D. Rutenberg. Fast and accurate coarsening simulation with an unconditionally stable time step. Phys. Rev. E, 68:0066703-0066716, 2003.
[35] Y. Wang and A.G. Khachaturyan. Three-dimensional field model and computer modeling of martensitic transformations. Acta Mater., 45:759-773, 1997.
[36] Y. Wang, L.Q. Chen and A.G. Khachaturyan. Kinetics of strain-induced morphological transformation in cubic alloys with a miscibility gap. Acta Metall. Mater., 41:279-296, 1993.
[37] Y. Wang and J. Li. Phase field modeling of defects and deformation. Acta Metall. Mater., 58:1212-1235, 2010.
[38] X.P. Wang, C.J. Garcia-Cervera and W. E. A Gauss-Seidel projection method for micromagnetics simulations. J. Comput. Phys., 171:357-372, 2001.
[39] H. Wu, S.M. Wise, C. Wang and J.S. Lowengrub. Stable and efficient finite-difference nonlinear-multigrid schemes for the phase field crystal equation. J. Comput. Phys., 228:5323-5339, 2009.
[40] C. Xu and T. Tang. Stability analysis of large time-stepping methods for epitaxial growth models. SIAM J. Numer. Anal., 44:1759-1779, 2006.
[41] L. Zhang, L.-Q. Chen and Q. Du. Diffuse-interface description of strain-dominated morphology of critical nuclei in phase transformations. Acta Metall. Mater., 56:3568-3576, 2008.
[42] L. Zhang, L.-Q. Chen and Q. Du. Mathematical and numerical aspects of a phase-field approach to critical nuclei morphology in solids. J. Sci. Comput., 37:89-102, 2008.
[43] L. Zhang, L.-Q. Chen and Q. Du. Simultaneous prediction of morphologies of a critical nucleus and an equilibrium precipitate in solids. Commun. Comput. Phys., 7:674-682, 2010.
[44] J. Zhu, L.-Q. Chen and J. Shen. Morphological evolution during phase separation and coarsening with strong inhomogeneous elasticity. Modelling Simul. Mater. Sci. Eng., 9:499-511, 2001.